Numerical and Experimental Study of a Novel Compact Micro Fluidized Beds Reactor for CO_2 Capture in HVAC

Xiaofei Li[1,2], Lei Wang[1,*], Lei Jia[1,**], Wenjian Cai[2]

[1] School of Control Science and Engineering, Shandong University, Jinan 250061, P. R. China
[2] School of Electrical and Electronic Engineering, Nanyang Technological University, Singapore 639798, Singapore

Abstract: In order to reduce the pressure drop and increase the adsorption performance for the CO_2 capture using solid adsorbents in Heating, Ventilation and Air Conditioning (HVAC), a novel Compact Micro Fluidized Beds (CMFB) reactor was proposed. First, the pressure drop and adsorbent attrition of the CMFB reactor were calculated by Eulerian-Lagrangian Computational Particle-Fluid Dynamics (CPFD) modelling with Barracuda software and compared with traditional Fluidized Bed (FB) reactor. Second, a CMFB experimental platform was designed based on the CPFD model. At last, the pressure drop, adsorbent attrition and performance for CO_2 capture were systematically investigated in the CMFB experimental platform. The results showed that much lower pressure drop and lower adsorbent attrition were achieved by CMFB reactor than by FB reactor due to large inlet area and reduced feed velocity. The CMFB reactor can gain long-term energy-saving effects in HVAC. Furthermore, the breakthrough time increased by about 35% and the saturation time reduced by about 17% in CMFB reactor for CO_2 capture than that in FB reactor.

Keywords: CO_2; adsorption; HVAC; fluidized bed;

Nomenclature	
C_d	Drag coefficient
D_p	Interphase drag coefficient (1/s)
$\boldsymbol{F}$	Rate of momentum exchange per volume between the gas and particle phases (N/m^3s)
f	Probability distribution function
g	Gravitational acceleration (m/s^2)
I_p	Magnitude of the impact value ($kg^a \cdot m^b/s^b$)
m_p	Particle mass (kg/m^3)
n_p	Number of particles in a numerical particle
N_p	Number of numerical particles
p	Gas pressure (Pa)

Corresponding author: * E-mail: leiwang@sdu.edu.cn, Tel: +86 531 8839 3598; ** E-mail: jialei@sdu.edu.cn, Tel: +86 531 8839 3598.

P_s	Positive constant (Pa)
r_p	Particle radius (m)
Re	Reynolds number
S	Interpolation operator
t	Time (s)
$\boldsymbol{u}_\mathrm{g}$	Gas velocity (m/s)
$\boldsymbol{u}_\mathrm{p}$	Particle velocity (m/s)
U	Superficial gas velocity (m/s)
V	Volume
w	Weighting factor
$\boldsymbol{x}_\mathrm{p}$	Particle location (m)
Greek letters	
ρ	Density (kg/m^3)
θ	Volume fraction
τ	Viscous stress tensor (N^2/m^2)
μ	Gas viscosity (Pa·s)
ε	Constant number
β	Constant number
Subscriptions	
cp	Close pack
g	Gas
p	Particle

1. Introduction

Efficient and cost-effective CO_2 capture is of great importance in various applications pertaining to environment, cryogenic air separation and personal confined spaces such as submarines, aerospace shuttles and some buildings [1,2]. In recent years, a lot of attentions have been devoted to design the CO_2 capture reactor system using solid adsorbents which can be combined into the central air conditioning in buildings [3-5].

The adsorption reactor, as one of the key equipments of CO_2 capture system, is used for contacting CO_2-laden gas streams with solid adsorbents. Therefore, the study of efficient and cost-effective adsorption reactor is very important for CO_2 capture in Heating, Ventilation and Air Conditioning (HVAC). At present, many kinds of reactors have been applied in the field of CO_2 capture using solid adsorbents, such as fixed bed, moving bed and fluidized bed reactors [6-9]. Fixed and moving beds have poor heat transfer and great diffusional resistance [10]; fluidized beds have the advantages of excellent gas-solid contact, minimum diffusional resistance and superior mass and heat transfer characteristics. Fluidized beds are likely to be superior to the fixed and moving beds [11].

Fluidized beds have been applied widely in a variety of industrial processes at conventional scales ranging from decimeters to meters [12,13]. In recent years, there is a growing interest in the miniaturization of fluidized beds, because micro-scale fluidized beds have the advantage of high heat and mass transfer efficiency, reduced pressure drop, good mixing of reactant and catalyst, improved safety, and other specific required characteristics [14,15]. Applications of micro fluidized bed have been reported, such as the Macro-scale Photocatalytic Fluidized Bed Reactor (MPFBR) [16], the Micro Fluidized Bed Reaction Analyzer (MFBRA) [17], the Micro Membrane Fluidized Bed Reactor (MMFBR) [14] and other micro-structured fluidized beds [18,19].

Potic et al. [20] first introduced the concept of micro fluidized beds as referring to beds with inner diameters of a few millimeters. Liu et al. [21] investigated the fluidization characteristics of gas-solid micro fluidized beds. The minimum fluidization velocity in gas-solid micro fluidized beds were studied by Guo et al. [22]. Recently, Wang and Fan [23] carried out a series of gas-solid fluidization experiments using fluid catalytic cracking (FCC) particles in micro-channels. Doroodchi et al. [19] examined the hydrodynamics of three liquid-solid micro fluidized beds. In addition to the experimental studies, computational particle fluid dynamics (CPFD) has been extensively used to improve understanding of fluidized beds and micro fluidized beds in terms of minimum fluidization velocity and bed expansion characteristics [24-26]. Wang et al. [14] found that a micro-structured fluidized bed reactor can be operated in turbulent fluidization regime with much lower gas flow rates compared with bigger scale fluidized bed reactors by numerical simulations. Snider et al. [27] presented application of the hybrid Euler-Lagrange method for modeling the gasification process in large industrial fluidized bed reactors. Lim et al. [28] carried out CPFD simulations in bubbling fluidized beds, and they found that bed pressure drops are similar to those obtained from experimental data.

At present, nearly all the previous studies were about the fluidization characteristics of single micro fluidized bed containing very small amounts of bed materials, but multiple micro fluidized beds used together in one reactor for scale-up application was rarely involved. A suitable CO_2 capture reactor which can meet the designed constraints of low pressure drop, high adsorption performance and low adsorbent attrition under high air flow is urgently needed to develop in HVAC.

In this study, a novel CMFB reactor was proposed to meet the requirements of HVAC. The pressure drop and particle attrition in the CMFB and FB reactors were simulated by CPFD model. The performance of the CMFB and FB reactors in terms of pressure drop, CO_2 adsorption and adsorbent attrition were investigated experimentally. The CPFD simulation data are compared with the experimental results in the CMFB reactor, and compared with that in the FB reactor.

2. CPFD mathematical model

2.1. Governing equations

The CPFD methodology takes an Eulerian-Lagrangian approach to describe the gas-solid flow in three dimensions. The gas phase is described as continua by averaged Navier-Stokes equations and the solid phase is modeled as discrete particle. The gas phase is strongly coupled with the discrete particles phase in mass, momentum and energy conservation equations. The particle momentum description follows the multi-phase particle-in-cell (MP-PIC) numerical method, which provides a Lagrangian description of particle motion coupled with the gas by ordinary differential equations [29]. As there is no reaction and interphase mass transfer, no gas phase energy equations are needed. For the gas phase, the volume averaged gas mass and momentum equations are

$$\frac{\partial \theta_{\mathrm{g}} \rho_{\mathrm{g}}}{\partial t} + \nabla \cdot \left(\theta_{\mathrm{g}} \rho_{\mathrm{g}} \mathbf{u}_{\mathrm{g}} \right) = 0 \tag{1}$$

$$\frac{\partial \left(\theta_{\mathrm{g}} \rho_{\mathrm{g}} \mathbf{u}_{\mathrm{g}} \right)}{\partial t} + \nabla \cdot \left(\theta_{\mathrm{g}} \rho_{\mathrm{g}} \mathbf{u}_{\mathrm{g}} \mathbf{u}_{\mathrm{g}} \right) = -\nabla p + \nabla \cdot \left(\theta_{\mathrm{g}} \tau_{\mathrm{g}} \right) + \theta_{\mathrm{g}} \rho_{\mathrm{g}} g - \mathbf{F} \tag{2}$$

where $\boldsymbol{u}_{\mathrm{g}}$, ρ_{g}, θ_{g}, p, τ_{g}, and g are the gas velocity, the gas density, the gas volume fraction, the gas pressure, the gas stress tensor and the gravitational acceleration, respectively. $\boldsymbol{F}$ is the rate of momentum exchange per volume between the gas and particle phases.

$$\mathbf{F} = \iint f m_{\mathrm{p}} \left(D_{\mathrm{p}} \left(\mathbf{u}_{\mathrm{g}} - \mathbf{u}_{\mathrm{p}} \right) - \frac{1}{\rho_{\mathrm{p}}} \nabla p \right) dm_{\mathrm{p}} d\mathbf{u}_{\mathrm{p}} \tag{3}$$

where f, m_{p}, D_{p}, $\boldsymbol{u}_{\mathrm{p}}$ and ρ_{p} are the particle distribution function, the particle mass, the interphase drag coefficient, the particle velocity and the particle density, respectively.

For the particle phase, the particles are modeled using the Lagrangian method with the numerical particles each containing n_p particles with identical properties located at position $\boldsymbol{x}_\mathrm{p}$ (x_p, y_p, z_p). The particle acceleration is

$$\frac{d\mathbf{u}_\mathrm{p}}{dt} = D_\mathrm{p}\left(\mathbf{u}_\mathrm{g} - \mathbf{u}_\mathrm{p}\right) - \frac{1}{\rho_\mathrm{p}}\nabla p + g - \frac{1}{\theta_\mathrm{p}\rho_\mathrm{p}}\nabla\tau_\mathrm{p} \tag{4}$$

where θ_p and τ_p are the volume fraction of particles and the particle normal stress.

The particle movement is given by

$$\frac{d\mathbf{x}_\mathrm{p}}{dt} = \mathbf{u}_\mathrm{p} \tag{5}$$

2.2. Interphase drag model

The interphase drag model used here is [29]

$$D_\mathrm{p} = C_\mathrm{d}\frac{3}{8}\frac{\rho_\mathrm{g}}{\rho_\mathrm{p}}\frac{\left|\mathbf{u}_\mathrm{g} - \mathbf{u}_\mathrm{p}\right|}{r_\mathrm{p}} \tag{6}$$

where

$$C_\mathrm{d} = \frac{24}{\mathrm{Re}}\left(1 + 0.15\,\mathrm{Re}^{0.687}\right)\theta_\mathrm{g}^{-2.65} \qquad \mathrm{Re} < 1000 \tag{7}$$

$$C_\mathrm{d} = 0.44\theta_\mathrm{g}^{-2.65} \qquad \mathrm{Re} \geq 1000 \tag{8}$$

$$\mathrm{Re} = \frac{2\rho_\mathrm{g}\left|\mathbf{u}_\mathrm{g} - \mathbf{u}_\mathrm{p}\right|}{\mu_\mathrm{g}}\left(\frac{3V_\mathrm{p}}{4\pi}\right)^{1/3} \tag{9}$$

where μ_g and V_p is the gas viscosity and the particle volume.

2.3. Particle stress model

In the CPFD scheme, the particle-particle collisions are modeled by the particle normal stress [29], which is given by

$$\tau_\mathrm{p} = \frac{P_\mathrm{s}\theta_\mathrm{p}^{\beta}}{\max\left[\left(\theta_\mathrm{cp} - \theta_\mathrm{p}\right), \varepsilon\left(1 - \theta_\mathrm{p}\right)\right]} \tag{10}$$

where P_s is a positive constant and θ_cp is the particle volume fraction at close packing. β and ε are dimensionless constants. β is recommended to be 2 - 5.

2.4. Attrition model

In CPFD model, the particle attrition caused by single particle-wall collision is calculated by the following expression:

$$I_{\mathrm{p}} = w\left(\alpha_{\mathrm{p}}\right)\cdot m_{\mathrm{p}}^{a}\cdot \mathbf{u}_{\mathrm{p}}^{b} \tag{11}$$

where $w(\alpha_{\mathrm{p}})$ is the weighting factor which is a function of the impact angle α_{p}. Exponents a and b are constants. In this study, $w(\alpha_{\mathrm{p}})$ is left default, the mass exponent a and particle velocity exponent b are left to be 1 and 2 [30].

2.5. Numerical solution

The flow diagram of the different modules that constitute the CPFD model and the variables that are exchanged between the modules are displayed in Fig. 1. In the CPFD approach, the particle properties are mapped from the Eulerian grid to the particle locations. The particle properties are also then mapped from the particles to the grid to get grid-based properties. Each grid cell contains numbers of numerical particles. The particle volume fraction at cell ξ from mapping particle volume to the grid is

$$\theta_{\mathrm{p}\xi} = \frac{1}{V_{\xi}}\sum_{1}^{N_{\mathrm{P}}} n_{\mathrm{p}} V_{\mathrm{p}} S_{\mathrm{p}\xi} \tag{12}$$

where V_{ξ}, N_{p}, n_{p} and $S_{\mathrm{p}\xi}$ are the volume of cell ξ, the total number of numerical particles in the cell, the number of real particles in a numerical particle and the interpolation operator, respectively. The sum of the gas and particle volume fractions must equal unity, $\theta_{\mathrm{p}} + \theta_{\mathrm{g}} = 1$, which is used to solve gas continuity and momentum equations in the next time step.

The mass and momentum equations are approximated and solved by finite volumes with staggered scalar and momentum nodes. The numerical particle velocity at the following time step is updated from integration of Eq. (4).

$$\mathbf{u}_{\mathrm{p}}^{n+1} = \frac{\mathbf{u}_{\mathrm{p}}^{n} + \Delta t\left[D_{\mathrm{p}}\mathbf{u}_{\mathrm{g,p}}^{n+1} - \frac{1}{\rho_{\mathrm{p}}}\nabla p_{\mathrm{p}}^{n+1} - \frac{1}{\rho_{\mathrm{p}}\theta_{\mathrm{p}}}\nabla \tau_{\mathrm{p}}^{n+1} + g\right]}{1 + \Delta t D_{\mathrm{p}}} \tag{13}$$

where $\boldsymbol{u}_{\mathrm{g,p}}^{n+1}$, $\nabla p_{\mathrm{p}}^{n+1}$ and $\nabla\tau_{\mathrm{p}}^{n+1}$ are the interpolated gas velocity, the interpolated pressure gradient and the interpolated particle stress gradient at the particle location, respectively.

The new particle location at the next time step is

$$\mathbf{x}_{\mathrm{P}}^{n+1} = \mathbf{x}_{\mathrm{P}}^{n} + \mathbf{u}_{\mathrm{P}}^{n+1}\Delta t \tag{14}$$

The gas momentum equation implicitly couples the gas and the particles by the interphase momentum transfer. The interphase momentum transfer at momentum cell ξ is

$$\mathbf{F}_{\xi}^{n+1}=\frac{1}{V_{\xi}}\sum_{1}^{N_{\mathrm{p}}}S_{\mathrm{p}\xi}\left[D_{\mathrm{p}}\left(\mathbf{u}_{\mathrm{g,p}}^{n+1}-\mathbf{u}_{\mathrm{p}}^{n+1}\right)-\frac{1}{\rho_{\mathrm{p}}}\nabla p_{\mathrm{p}}^{n+1}\right]n_{\mathrm{p}}m_{\mathrm{p}} \tag{15}$$

The summation is over all numerical particles N_{p} in the cell.

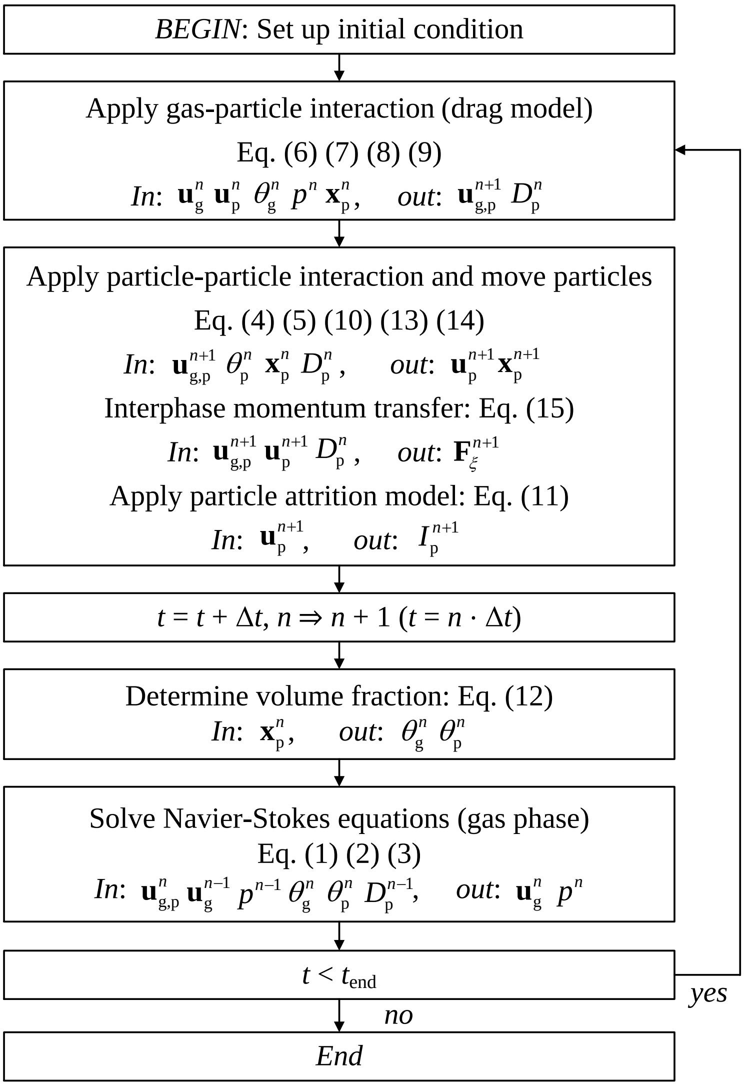

Fig. 1. Flow diagram of the CPFD mathematical model.

3. CMFB and FB reactors models

The three-dimensional CMFB and FB reactors were modeled with Barracudas CPFD software. The schematic diagram of the CMFB reactor model is depicted in Fig. 2. The CMFB reactor contains 100 micro fluidized beds. For every micro fluidized bed, the length and width were 10 mm, the height was 42 mm, the thickness of the bed wall was 0.75 mm and the distributor was made of a mesh with size of 0.1 mm. The particles used in the simulations were set as FCC particles which is the most similar material to the adsorbent used in the experiments in terms of physical characteristics in the material library of Barracudas software. The diameters and particle density of FCC particles were 300-500 μm and 1133 kg/m^3, respectively. The initial bed heights consisted of 120 g FCC particles of the CMFB and FB were 25 mm and 154 mm, and the bulk density was the same 680 kg/m^3. The particle close pack volume fraction was set as 0.6. Air was used as the fluidizing gas and the superficial velocities were ranging from 0 m/s to 1.59 m/s. Gas and particle properties and simulation conditions are listed in Table 1.

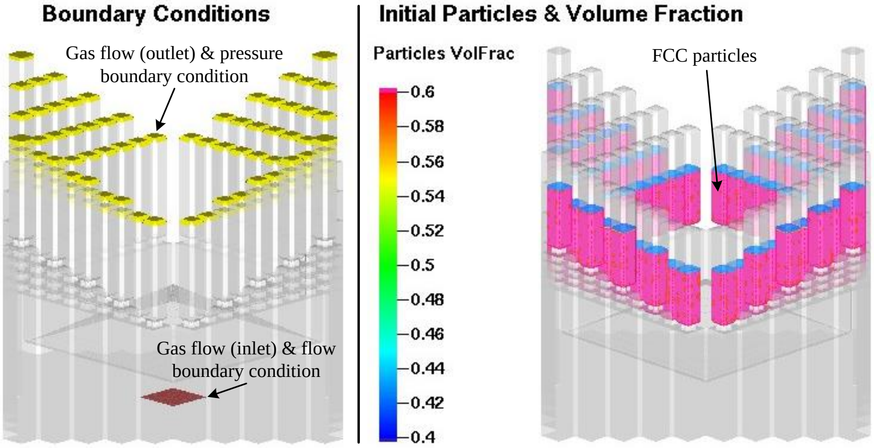

Fig. 2. Geometry of the CMFB reactor and initial conditions.

Table 1

Gas and solid properties and simulation conditions.

Gas	Ambient air (compressible)
Gas density (kg/m^3)	1.225
Superficial gas velocity (m/s)	0 - 1.59 (0 L/min - 30 L/min)
Particle	FCC particles
Particle density (kg/m^3)	1133
Bulk density (kg/m^3)	680
Particle diameter (μm)	300 - 500
Bed mass (g)	120
Initial bed height (mm)	25 (CMFB); 154 (FB)
Close pack volume fraction	0.6

The inlet boundary for the gas phase was at the bottom of the reactor where room temperature and atmospheric pressure were set. A constant atmospheric pressure boundary condition was employed at the top of the beds where the gas left through. The positions of the boundary conditions are also depicted in Fig. 2. The particle normal-to-wall momentum retention coefficient was 0.3, the tangent-to-wall retention coefficient was 0.99 and the diffuse bounce was 0, respectively. P_s, β and ε represent the constants for the particle normal stress model which were set at $P_s = 10$ Pa, $\beta = 3$ and $\varepsilon = 10^{-8}$ as recommended by Snider et al [29]. The simulations were performed until 30 s total simulation time and the last 25 s were taken for averaging. The input parameters for the CPFD simulations are presented in Table 2.

Table 2

Simulation parameters.

Particle-to-wall interaction	
Normal retention coefficient, e_n	0.3
Tangential retention coefficient, e_t	0.99
Diffuse bounce, D_f	0
Particle normal stress model	
Pressure constant of the solid-phase stress model, P_s	10 Pa
Dimensionless constant of the solid-phase stress model, β	3
Dimensionless constant of the solid-phase stress model, ε	10^{-8}
Maximum momentum redirection from collision	40%
Time settings	
Time step, Δt	0.001 s
Total time, t	30 s
Beginning time for average	5 s

4. Experiment

4.1. Experimental apparatus

The CMFB and FB reactors experimental platform were designed and built in accordance with the optimized geometry and operating conditions by the CPFD simulations described above. The schematic of the CMFB reactor is shown in Fig. 3 (a). The CMFB reactor consists of an enclosed cuboid housing section which was 130 mm, 130 mm, 250 mm in length, width and height respectively, and a CMFB section which was built by connecting 100 micro fluidized beds depicted in Fig. 2. The distributors were made of wire meshes with mesh size of 0.1 mm. At the bottoms of the reactors, two gas streams i.e. carbon dioxide and nitrogen with individual valves and mass flow controller were regulated to serve as the fluidizing gas or stripping gas. A series of temperature and pressure sensors are installed at different heights of the reactor walls for monitoring the fluidization behavior. CO_2 concentrations at the inlets and outlets of the reactors were continuously monitored by a mass spectrometer (MS). A photograph of the experimental platform is shown in Fig. 4.

To demonstrate the performance of the CMFB reactor, the FB reactor was used as the comparison reactor which was 350 mm in height and 38.5 mm in internal diameter shown schematically in Fig. 3 (b). The distributor was made of porous metal with averaged pore size of 0.1 mm and 3 mm thickness.

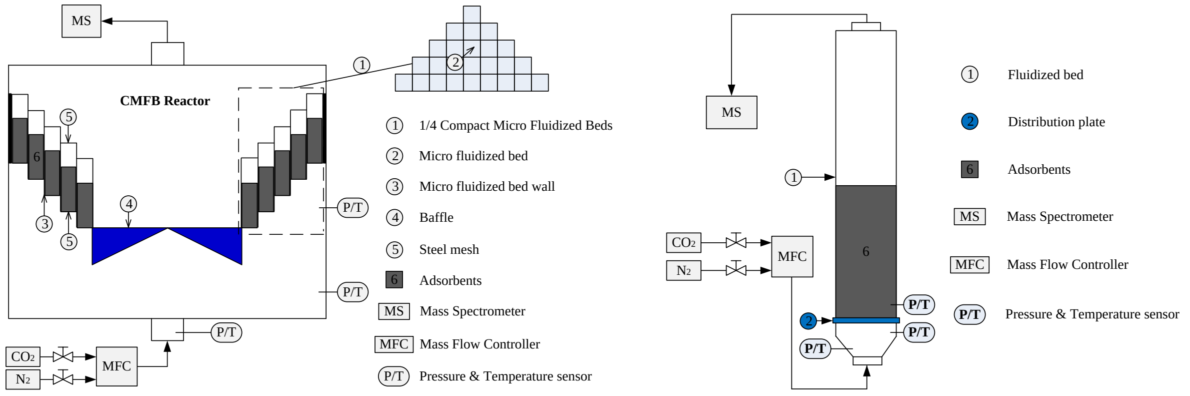

(a) (b)

Fig. 3. Schematics of the CMFB (a) and FB (b) reactors.

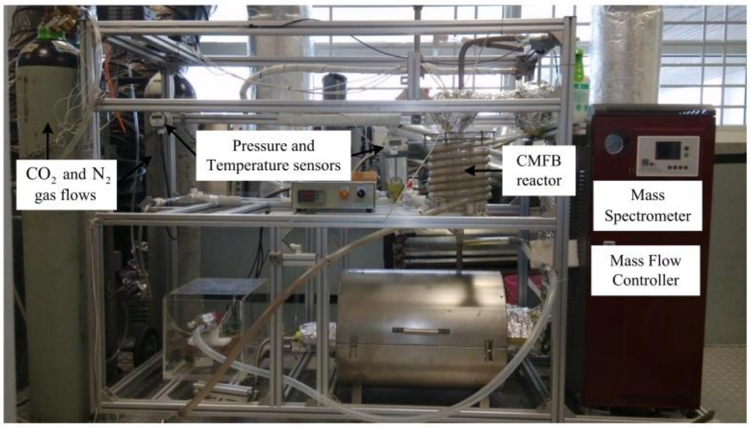

Fig. 4. The photograph of the experimental platform.

According to OSHA Standards promulgated by Occupational Safety and Health Administration of America, the CO_2 concentration limit exposed to the air in workplaces is 0.5%. The 0.5% CO_2/N_2 gas mixture was used as the fluidizing gas which was prepared from pure CO_2 (99.99%) balanced with pure N_2 (99.995%) controlled by a mass flow controller, and pure N_2 was used as the purging gas for adsorbent regeneration. The adsorbent used in this study was synthesized by impregnating a mass ratio of 50% polyethyleneimine (PEI) into a macroporous resin support which had a pore volumes of 0.15 cm^3/g. The PEI-resin adsorbents had the particle density and diameters of 1133 kg/m^3 and 300-500 μm, and exhibits excellent adsorption capacity of 93.5 mg/g for 0.5% CO_2/N_2 gas mixture [9].

4.2. Experimental process design

The pressure drop measurements were performed for the empty beds, ΔP_e, and the beds containing particles, ΔP_b. The pressure drop due to bed of particles, ΔP, was then calculated by: $\Delta P = \Delta P_b - \Delta P_e$. The average pressure drop over a period of 15 s (when the pressure drop was stable) was defined as the pressure drop at a given superficial gas velocity. During the experiment, the 0.5% CO_2/N_2 gas mixture was increased from 0 L/min to 30 L/min.

Before the adsorption experiment, the adsorbents was pretreated at 100 ℃ under flowing N_2 of 20 L/min for 60 min to remove the moisture and adsorbed CO_2 as much as possible. It was then cooled to the desired temperature and exposed to the 0.5% CO_2/N_2 gas mixture. The dynamic adsorption capacity (*q*) of the adsorbents is calculated using Eq. (16) [31]:

$$q = \frac{MC_{\mathrm{i}}}{W} \int_0^{\infty} \left(1 - \frac{C_{\mathrm{o}}}{C_{\mathrm{i}}}\right) dt \tag{16}$$

where M, W and t are the total molar flow, the mass of adsorbents and the time, respectively. C_{i} and C_{o} are the CO_2 concentrations of the inlet and outlet gas. The saturation adsorption capacity is calculated at the saturation time when C_{o} is equal to C_{i}, while the breakthrough adsorption capacity is calculated at the breakthrough time when C_{o} is 5% of C_{i}. The regeneration experiments were conducted by rapidly heating the beds to 100 ℃ in pure N_2 with a flow rate of 20 L/min, and then the CO_2 adsorbed by the adsorbents could be desorbed.

The adsorbent attrition was determined by the ratio between the loss mass and the initial mass of the adsorbents after 10 consecutive cycles of CO_2 adsorption/desorption experiments under the flow rate of 30 L/min in the CMFB and FB reactors. The particle size distribution of the fresh and attrite adsorbents was obtained from standard sieve analysis.

The experimental conditions of the pressure drop, the performance for CO_2 capture and the adsorbent attrition measurements are summarized in Table 3.

Table 3

Experimental conditions.

Experiment	Bed particles	Fluidizing gas	Superficial fluidizing velocity (m/s)
Pressure drop	PEI-resin adsorbents	0.5% CO_2/N_2	0 - 1.59 (0 - 30 L/min)
CO_2 adsorption		0.5% CO_2/N_2	1.06 (20 L/min)
Adsorbent regeneration		Pure N_2	1.06 (20 L/min)
Adsorbent attrition		0.5% CO_2/N_2	1.59 (30 L/min)

5. Results and Discussion

5.1. Pressure drop in CMFB and FB reactors

A proper identification of fluidization regimes is usually the first and key step towards the rational use of fluidized beds. The simulation snapshots of the cell vector magnitude and cell pressure drop of the bed containing particles, and the cell pressure drop of the empty bed in the CMFB reactor at U = 1.59 m/s (30 L/min) are shown in Fig. 5. It can be seen in the Fig. 5 (a) that the cell vector magnitudes distribute almost uniformly and equivalently after a special baffle was introduced in the CMFB reactor. The cell vector magnitudes in the distributor regions are much higher than the around regions. Fig. 5 (b) shows that the cell pressure drop of the empty bed at U = 1.59 m/s is only 4 Pa, which indicates that the cell pressure drop caused by the baffle can be ignored. Fig. 5 (c) indicates that the cell pressure at the bottom is always greater than the top one, and reduces gradually from the bottom to the top regions of every micro fluidized bed. Since the difference in dynamic pressure drop is proportional to the difference in bulk density, the data satisfy the elementary stability criterion according to which the bulk density must be a decreasing function of height.

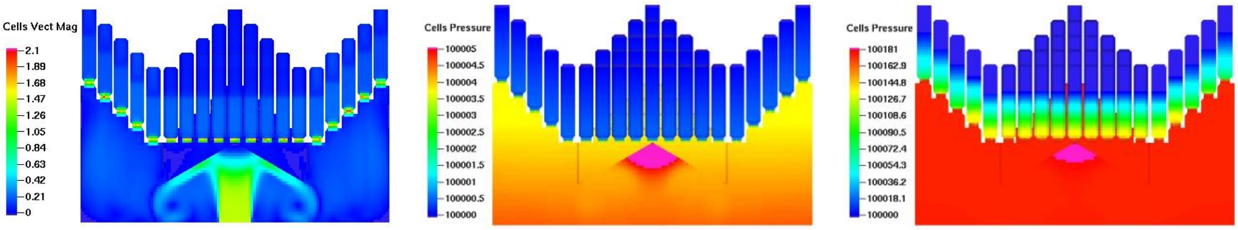

(a) (b) (c)

Fig. 5. Snapshots of the cell vector magnitude (a) and cell pressure drop (c) of the bed containing particles, and the cell pressure drop of the empty bed (b) in the CMFB reactor at U = 1.59 m/s.

The pressure drops in the CMFB and FB reactors varied with velocities were determined experimentally. Fig. 6 shows the typical pressure drop diagrams that indicate the linear increase with gas flow rates when the CMFB and FB are static and the subsequent levelling tendency irrespective of further increase in gas flow rates when the CMFB and FB have already been fluidized. In the same figure are plotted the pressure drops in the CMFB and FB reactors calculated from the simulation values. The transition points correspond to the minimum fluidization condition for the CMFB and FB with the flow rates being around 8.5 L/min and 2.0 L/min in the experiment and 10 L/min and 2.5 L/min in the simulation, respectively. It can be seen that the pressure drop in the fluidized CMFB is 175 Pa which is much lower than 1250 Pa in the fluidized FB in the experiment, and 165 Pa which is much lower than 1100 Pa in the fluidized FB in the simulation. The pressure drops obtained from the simulation and experiment in the CMFB reactor achieve reductions of 86% and 85% as compared with that in the FB reactor, respectively.

The pressure drop predicted by the CPFD model is greater than the one observed in the experiment both in the CMFB and FB reactors. The main probable reason for this is that the bed materials used in the experiment has a higher porosity which leads to larger gas-solid contact area compared with the bed materials used in the simulation. The pressure drops obtained from the simulation and experiment show a similar tendency and the reductions achieved from the simulation and experiment are almost equal. Compared with the FB reactor, a lower pressure drop can be achieved by the CMFB reactor due to the relatively large inlet area and the reduced feed velocity.

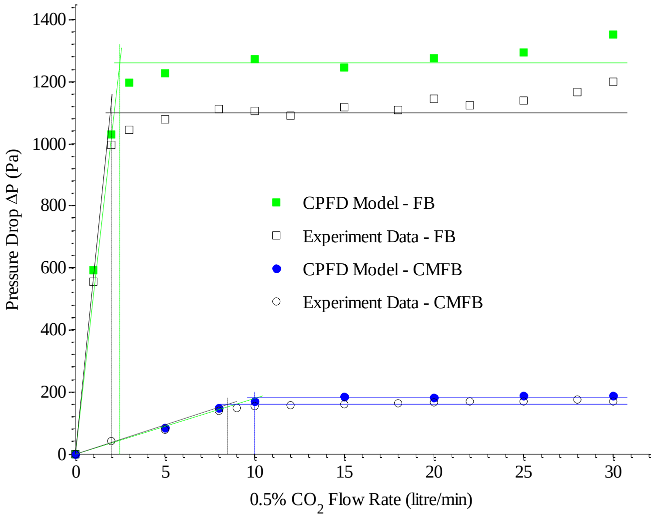

Fig. 6. Comparison of the simulation and experimental data of the pressure drops between the CMFB and FB reactors at different flow rates.

The pressure drops in the CMFB and FB reactors obtained by CPFD simulations and experiments in this study are compared with those in different fluidized beds reported in a few literatures, given in Table 4. Guo et al. [22] and Liu et al. [21] reported low pressure drops of around 240 Pa and 600 Pa in the MFBs using several milligrams particles at a very low flow rate respectively. A low pressure drop of around 620 Pa in a MFB at a relatively high flow rate was published by Dang et al. [15]. The MFBs reported in above literatures have low pressure drop, but can only be used at millimeter or centimeter scale. Zhang et al. [8] evaluated CO_2

capture from ambient air in a laboratory-scale bubbling fluidized bed using 1.0 kg adsorbents, and obtained a high pressure drop of around 2500 Pa at a low flow rate. Lim et al. [28] carried out CPFD simulations in a bubbling fluidized bed containing large amounts of particles at a high flow rate, and achieved a very high pressure drop of 9450 Pa. A very high pressure drop of 7500 Pa in a large-scale fluidized bed column was also published by Chen et al. [25]. Comparing with all the reference data listed in Table 4, the pressure drop in the proposed CMFB in this study is the lowest. The CMFB reactor has lower pressure drop which can reduce the resistance overcome by the gas supply apparatus and then save energy consumption for gas supply. The CMFB reactor can gain long-term energy-saving effects in removing CO_2 from indoor air cyclically in HVAC.

Further research on the systematic and long-term energy consumption for CO_2 capture from indoor air using the CMFB reactor in HVAC is still needed which should include the evaluation of the capital costs for equipment and adsorbent, and the energy consumption for CO_2 adsorption and adsorbent regeneration.

Table 4

Comparison of the pressure drops of the beds in the present study and in reported studies.

	Bed type, D_{bed}^{a} (mm)	Particles, D_p^{b} (μm)	M_{bed}^{c} (kg)	H_s^{d} (mm)	Gas,V_{gas}^{e} (L/min)	ΔP_{CPFD}^{f} (Pa)	$\Delta P_{expt.}^{g}$ (Pa)
CMFB	MFB[h] (100),	FCC (CPFD),		25	air(CPFD)	165	175
(present work)	8.5*8.5	PEI-resin(expt.),	0.12		0.5% CO_2		
FB (present work)	FB, 38.5	300-500		154	(expt.), 30	1100	1250
Guo et al. [22]	MFB, 10.5	FCC, 83	0.003	33	N_2, 0.6		240
Liu et al. [21]	MFB, 12	silica sand, 460.6	0.007	50	air, 1.4		600
Dang et al. [15]	FB, 10*40	glass beads, 400-600	0.04	80	air, 31		620
Zhang et al. [8]	FB, 67	PEI-silica, 250	1	410	air, 8		2500
Lim et al. [28]	FB, 300	MG-Si, 150	75	900	air, 720	9450	
Chen et al. [25]	FB, 300*1000	Geldart B, 140	245	588	air, 54000		7500

[a] bed diameter; [b] particle mean diameter; [c] bed mass; [d] static bed height; [e] gas volume flow rate; [f] pressure drop obtained by CPFD simulation; [g] pressure drop obtained by experiment; [h] micro fluidized bed.

5.2. Adsorbent attrition in the CMFB and FB reactors

The simulation snapshots of particles trauma, an attrition index which determine the particle attrition in the CPFD models are shown in Fig. 7. It can be seen that the particle trauma in the CMFB and FB are ranging from 0 to 1.4×10^{-6} and 0 to 8.6×10^{-6} respectively. The mean particle trauma in the CMFB is 2.4×10^{-7} which is much lower than 1.5×10^{-6} in the FB, as also listed in Table 5.

In the experiment, the change of the cumulative particle size distribution of the fresh and attrite PEI-resin adsorbents in the CMFB and FB are shown in Fig. 8. It is clear that the distribution band of attrite particle size in the FB shifts to the lower size limit much more than that in the CMFB. The fragmentation of particles by attrition in the FB is much active than that in the CMFB. The adsorbent attrition calculated from the adsorbents mass remainings which are 117.5 g in the CMFB and 107.1 g in the FB is listed in Table 5, and it can be seen that the adsorbent attrition is just 2.1% in the CMFB, which is much lower than 10.7% in the FB reactor. The FB reactor significantly increases adsorbent attrition and, thereby, the cost of adsorbent replacement.

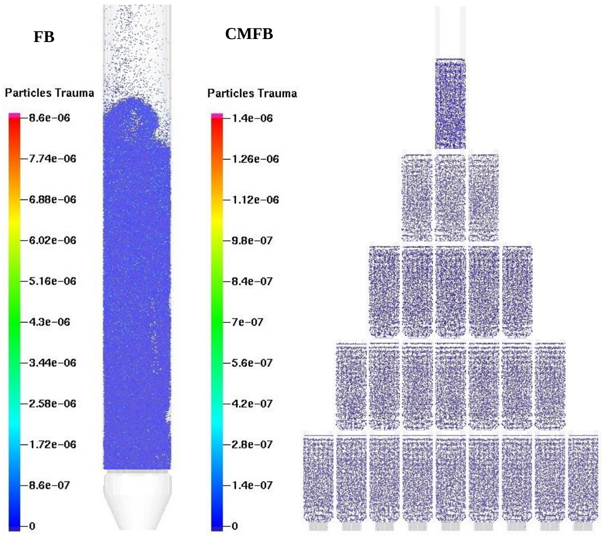

Fig. 7. Snapshots of the Particles Trauma in the CMFB and FB reactors.

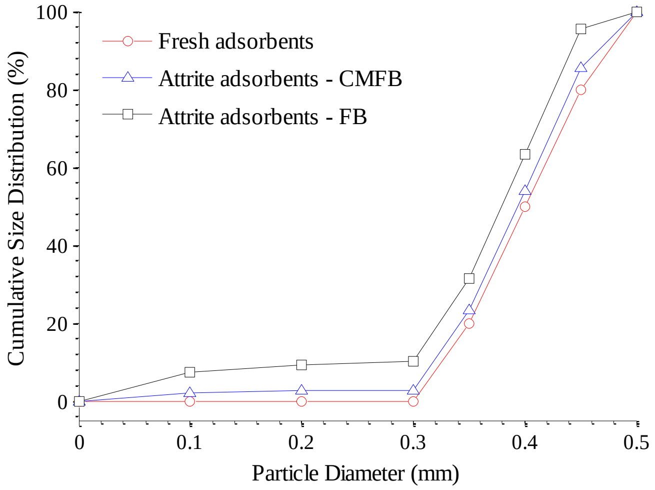

Fig. 8. Cumulative particle size distribution change in the CMFB and FB reactors.

Table 5

Experimental and modelling adsorbent attrition in the CMFB and FB reactors.

Reactors	Modelling adsorbent attrition (%)	Experimental adsorbent attrition (%)
CMFB reactor	2.4×10^{-7}	2.1
FB reactor	1.5×10^{-6}	10.7

5.3. Performance for CO_2 capture in the CMFB and FB reactors

During adsorption and desorption tests, a flow rate of 20 L/min was chosen in order to achieve fairly vibrant bubbling fluidization to facilitate sufficient gas-solid contact, mass transfer and heat transfer.

5.3.1. CO_2 adsorption performance

To demonstrate the superior performance of the CMFB reactor over the FB reactor, the breakthrough adsorption curve and saturated adsorption capacity of the PEI–resin adsorbent for 0.5% CO_2/N_2 gas mixture at the same flow rate were investigated in the CMFB and FB reactors respectively. As shown in Fig. 9, the CMFB reactor achieves a breakthrough time of about 0.84 h which is 35% larger than the 0.62 h in the FB reactor. The saturation adsorption time and capacities of about 2.73 h and 89.4 mg/g are achieved by the CMFB reactor, which is 17% shorter and 1.4% larger than about 3.31 h and 88.2 mg/g achieved by the FB reactor. These results suggest that the adsorbents can get more opportunities to contact with the gas, which increases the adsorbent utilization, accelerates overall kinetics and leads to a better adsorption performance for CO_2 capture in the CMFB reactor compared with that in the FB reactor.

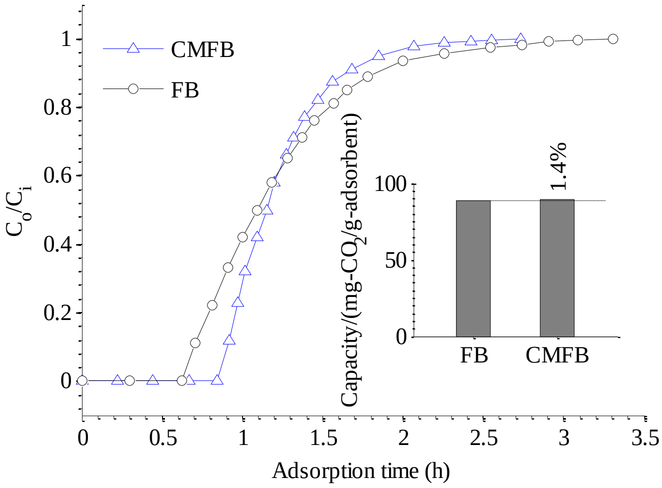

Fig. 9. Breakthrough adsorption curve and saturated adsorption capacity (inset) of the adsorbents in the CMFB and FB reactors.

5.3.2. Adsorbent regeneration

During the desorption experiments, the CO_2 concentrations of the outlet gases as a function of regeneration time are presented in Fig. 10. Nearly all of the CO_2 has been desorbed during 43 min in the CMFB reactor which is 17% less than the regeneration time of 52 min in the FB reactor. It can be seen that a rapid desorption provided by the CMFB reactor, indicating better gas-solid contact and superior heat-transfer characteristics than the FB reactor.

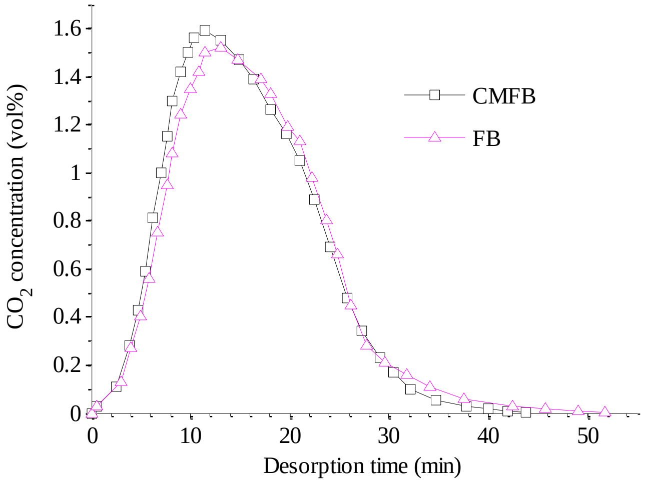

Fig. 10. Profiles of CO_2 concentration during desorption in the CMFB and FB reactors.

6. Conclusions

In this paper, a novel CMFB reactor was proposed for CO_2 capture in HVAC. The performance of the CMFB reactor was systematically studied with the CPFD model and experiment and compared with the FB reactor in terms of pressure drop, adsorbent attrition and performance for CO_2 capture. The main conclusions can be summarized as follows.

(1) The CMFB reactor is able to achieve a large inlet area and a relatively low inlet velocity, thus yielding a low pressure drop. The pressure drop reductions of 86% in the experiment and 85% in the simulation are achieved as compared with that in the FB reactor. The CMFB reactor can gain long-term energy-saving effects in HVAC.

(2) After ten cycles of CO_2 adsorption/desorption experiments, lower adsorbent attrition of 2.1% is achieved in the CMFB reactor, than 10.7% in the FB reactor due to the reduced feed velocity.

(3) The CMFB reactor achieves a breakthrough time 35% larger and a saturation adsorption time 17% shorter than that of the FB reactor. It demonstrates a better adsorbent utilization by the CMFB reactor due to a longer contact time caused by a lower velocity.

(4) The CMFB reactor provides a regeneration time 17% less than that in the FB reactor. It demonstrates a rapid desorption in the CMFB reactor due to a superior gas-solid contact.

This proposed CMFB reactor can be a competitive and promising adsorption reactor for CO_2 capture using solid adsorbents in HVAC applications.

Acknowledgements

This study was funded by the Fundamental Research Funds of Shandong University: 2014JC022. The other project partners are also acknowledged.

References

[1] A. Goeppert, M. Czaun, G.K.S. Prakash, G.A. Olah, Air as the renewable carbon source of the future: an overview of CO_2 capture from the atmosphere, Energy & Environmental Science. 5(7) (2012) 7833-7853.

[2] Y. Fan, K. Kameishi, S. Onishi, K. Ito, Field-based study on the energy-saving effects of CO_2 demand controlled ventilation in an office with application of energy recovery ventilators, Energy and buildings. 68 (2014) 412-422.

[3] Q. Wang, J. Luo, Z. Zhong, A. Borgna, CO_2 capture by solid adsorbents and their applications: current status and new trends, Energy & Environmental Science. 4(1) (2011) 42-55.

[4] A. Emeakaroha, C.S. Ang, Y. Yan, T. Hopthrow, A persuasive feedback support system for energy conservation and carbon emission reduction in campus residential buildings, Energy and Buildings. 82

(2014) 719-732.

[5] M.K. Kim, L. Baldini, H. Leibundgut, J.A. Wurzbacher, N. Piatkowski, A novel ventilation strategy with CO_2 capture device and energy saving in buildings, Energy and Buildings. 87 (2015) 134-141.

[6] F.N. Ridha, V. Manovic, A. Macchi, E.J. Anthony, CO_2 capture at ambient temperature in a fixed bed with CaO-based sorbents, Applied Energy. 140 (2015) 297-303.

[7] Y. Son, K. Kim, K.S. Lee, Feasibility study of a moving-bed adsorption process with heat integration for CO_2 capture through energy evaluation and optimization, Energy & Fuels. 28(12) (2014) 7599-7608.

[8] W. Zhang, H. Liu, C. Sun, T.C. Drage, C.E. Snape, Capturing CO_2 from ambient air using a polyethyleneimine–silica adsorbent in fluidized beds, Chemical Engineering Science. 116 (2014) 306-316.

[9] J. Wang, M. Wang, W. Li, W. Qiao, D. Long, L. Ling, Application of polyethylenimine-impregnated solid adsorbents for direct capture of low-concentration CO_2, AIChE Journal. 61(3) (2015) 972-980.

[10] W.C. Yang, J. Hoffman, Exploratory design study on reactor configurations for carbon dioxide capture from conventional power plants employing regenerable solid sorbents, Industrial & Engineering Chemistry Research. 48(1) (2008) 341-351.

[11] A. Samanta, A. Zhao, G.K.H. Shimizu, P. Sarkar, R. Gupta, Post-combustion CO_2 capture using solid sorbents: a review, Industrial & Engineering Chemistry Research. 51(4) (2011) 1438-1463.

[12] P. Ammendola, F. Raganati, R. Chirone, Effect of operating conditions on the CO_2 recovery from a fine activated carbon by means of TSA in a fluidized bed assisted by acoustic fields, Fuel Processing Technology. 134 (2015) 494-501.

[13] E.R. Monazam, J. Spenik, L.J. Shadle, Fluid bed adsorption of carbon dioxide on immobilized polyethylenimine (PEI): Kinetic analysis and breakthrough behavior, Chemical engineering journal. 223 (2013) 795-805.

[14] J. Wang, L. Tan, M.A. Van der Hoef, M. van Sint Annaland, J.A.M. Kuipers, From bubbling to turbulent fluidization: Advanced onset of regime transition in micro-fluidized beds, Chemical engineering science. 66(9) (2011) 2001-2007.

[15] N.T.Y. Dang, F. Gallucci, M. van Sint Annaland, An experimental investigation on the onset from bubbling to turbulent fluidization regime in micro-structured fluidized beds, Powder Technology. 256 (2014) 166-174.

[16] Z. Yang, M. Liu, C. Lin, Photocatalytic activity and scale-up effect in liquid–solid mini-fluidized bed reactor, Chemical Engineering Journal. 291 (2016) 254-268.

[17] J. Yu, X. Zeng, J. Zhang, M. Zhong, G. Zhang, Y. Wang, G. Xu, Isothermal differential characteristics of gas–solid reaction in micro-fluidized bed reactor, Fuel. 103 (2013) 29-36.

[18] J. Yu, X. Zeng, G. Zhang, J. Zhang, Y. Wang, G. Xu, Kinetics and mechanism of direct reaction between CO_2 and $Ca(OH)_2$ in micro fluidized bed, Environmental science & technology. 47(13) (2013) 7514-7520.

[19] E. Doroodchi, Z. Peng, M. Sathe, E. Abbasi-Shavazi, G.M. Evans, Fluidisation and packed bed

behaviour in capillary tubes, Powder technology. 223 (2012) 131-136.

[20] B. Potic, S.R.A. Kersten, M. Ye, M.A. van der Hoef, J.A.M. Kuipers, W.P.M. van Swaaij, Fluidization with hot compressed water in micro-reactors, Chemical Engineering Science. 60(22) (2005) 5982-5990.

[21] X. Liu, G. Xu, S. Gao, Micro fluidized beds: Wall effect and operability, Chemical Engineering Journal. 137(2) (2008) 302-307.

[22] Q. Guo, Y. Xu, X. Yue, Fluidization Characteristics in Micro-Fluidized Beds of Various Inner Diameters, Chemical engineering & technology. 32(12) (2009) 1992-1999.

[23] F. Wang, L.S. Fan, Gas-Solid Fluidization in Mini-and Micro-channels, Industrial & Engineering Chemistry Research. 50(8) (2011) 4741-4751.

[24] V. Vivacqua, S. Vashisth, G. Hébrard, J.R. Grace, N. Epstein, Characterization of fluidized bed layer inversion in a 191-mm-diameter column using both experimental and CPFD approaches, Chemical engineering science. 80 (2012) 419-428.

[25] C. Chen, J. Werther, S. Heinrich, H. Qi, E. Hartge, CPFD simulation of circulating fluidized bed risers, Powder technology. 235 (2013) 238-247.

[26] Y. Liang, Y. Zhang, T. Li, C. Lu, A critical validation study on CPFD model in simulating gas–solid bubbling fluidized beds, Powder Technology. 263 (2014) 121-134.

[27] D.M. Snider, S.M. Clark, P.J. O'Rourke, Eulerian–Lagrangian method for three-dimensional thermal reacting flow with application to coal gasifiers, Chemical engineering science. 66(6) (2011) 1285-1295.

[28] J.H. Lim, K. Bae, J.H. Shin, J.H. Kimb, D.H. Lee, J.H. Han, D.H. Lee, Effect of particle–particle interaction on the bed pressure drop and bubble flow by computational particle-fluid dynamics simulation of bubbling fluidized beds with shroud nozzle, Powder Technology. 288 (2016) 315-323.

[29] D.M. Snider, An incompressible three-dimensional multiphase particle-in-cell model for dense particle flows, Journal of Computational Physics. 170(2) (2001) 523-549.

[30] Y. Liang, Y. Zhang, C. Lu, CPFD simulation on wear mechanisms in disk–donut FCC strippers, Powder Technology. 279 (2015) 269-281.

[31] R. Serna-Guerrero, A. Sayari, Modeling adsorption of CO_2 on amine-functionalized mesoporous silica. 2: Kinetics and breakthrough curves, Chemical Engineering Journal. 161(1) (2010) 182-190.